

Article

# Oxygen Vacancy Enhanced Photoreduction Cr(VI) on Few-Layers BiOBr Nanosheets

Yin Peng \*, Pengfei Kan, Qian Zhang and Yinghua Zhou \*

The Key Laboratory of Functional Molecular Solids, Ministry of Education, College of Chemistry and Materials Science, Anhui Normal University, Wuhu 241000, China; 17855951090@163.com (P.K.); 19855351872@163.com (Q.Z.)

\* Correspondence: kimipeng@mail.ahnu.edu.cn (Y.P.); yhzhou@ahnu.edu.cn (Y.Z.);  
Tel.: +0553-3937135 (Y.P. & Y.Z.)

Received: 24 April 2019; Accepted: 11 June 2019; Published: 21 June 2019



**Abstract:** 2D nanomaterials, with unique structural and electronic features, had been demonstrated as excellent photocatalysts, whose catalytic properties could be tunable with surface defect engineering. In this work, few-layer BiOBr nanosheets with oxygen vacancies (BiOBr-Ov) have been fabricated by a simple solvothermal reaction with the help of ethylene glycol. The obtained BiOBr-Ov exhibited the superior photocatalytic performance with a complete reduction of Cr(VI) (20 mg/L) within 12 min by visible light irradiation. Moreover, Cr(VI) with a high concentration (such as 30 mg/L) only requires 2 min to be photoreduced completely under solar light irradiation. The enhanced photocatalytic performance is contributed to the existence of oxygen vacancies. It has been proved by the results of electrochemical impedance and photocurrent that oxygen vacancies can effectively suppress recombination of photogenerated carriers.

**Keywords:** oxygen vacancy engineering; photoreduction Cr(VI); BiOBr nanosheets

## 1. Introduction

Photocatalysis is able to directly convert solar light into chemical energy, being identified as a promising technology to solve environmental problems and the energy issues [1–5]. Despite exploring many photocatalysts and achieving numerous advancements, it is a far way to meet with the requirements of the practical application, due to the low photocatalytic efficiency and the poor stability. In order to boost the photocatalytic performance, there are adopted various strategies such as heterostructure, crystal facet exposure, doping, the engineered defects, dimension tuning, etc. [6–12]. Recently, Wang et al. demonstrated that excitons could be effectively dissociated into charge carriers with the incorporation of oxygen vacancy, leading to excellent performances in superoxide generation and selective organic syntheses under visible-light illumination [13].

2D nanomaterials with few-layers have emerged as a promising application in the photocatalytic field [14–17], by virtue of the optimal intrinsic properties or/and emerging behaviors induced by the high anisotropy, powerful quantum confinement effect and the surface defect [18]. In comparison with their bulk counterparts, the ultrathin 2D materials possess some superior advantages with the merit of the unique atomic structure [19]. For example, the large surface area could be propitious to the efficient light harvesting, the short charge diffusion distance from bulk to surface could decrease the photogenerated-carriers recombination, the rich coordination-unsaturated atoms at the surface could accelerate the interfacial redox reaction [20], and a low atomic-escape energy could be beneficial to constructing the atom-vacancies by the surface-atomic escape from crystal lattice [21]. Therefore, it is highly desirable to design the few layer 2D materials as photocatalysts to boost the catalytic performance.

The tetragonal BiOBr is a typical layered structure, which makes it beneficial to obtain few or atom layers [22]. It should be noted that the oxygen vacancies on BiOBr could be achieved by exposing the (001) crystal facets with the more high-density oxygen atom, resulting in the higher defect levels and thus regulating the structure of the electronic band, expanding the light absorption with the redshift [23–28]. In addition, oxygen vacancies could act as the trapping sites by capturing photogenerated holes or electrons, which would be helpful to the separation of carriers. Moreover, oxygen vacancy can effectively boost the adsorption and thus activate the gas molecules (such as O<sub>2</sub>, N<sub>2</sub>, H<sub>2</sub>O, CO<sub>2</sub>) [24]. Additionally, density functional theory (DFT) calculations [22] discover that an increased density of states (DOS) can be created at the conduction-band edge in the presence of oxygen vacancies compared with the BiOBr bulk, accelerating electron transport. Recently, few- or atom-layers BiOBr with oxygen vacancies have been reported, and these BiOBr exhibit good photocatalytic performance for photoreduction of CO<sub>2</sub> [22,25], photocatalytic nitrogen fixation [24,26], and degradation of organic compounds [27]. However, the study on the photoreduction of Cr(VI) catalyzed by few-layers BiOBr with oxygen vacancies has not been reported.

It is well known that the Cr(VI) species as a highly toxic and mutagenic reagent is detrimental to the environment and human beings [29,30]. The Cr(VI) species universally exists in the industrial wastewater, such as paint fabrication, textile manufacturing, leather tanning, steel fabrication, petroleum refining, and so on [31–34]. Therefore, the chemical reduction of Cr(VI) to Cr(III) is an essential key to be resolved. However, due to the limitation of the incomplete precipitation, sludge production and high operating costs, it is still an embarrassing circumstance to utilize the traditional methods of removing Cr(VI), such as ion exchange, bioremediation, membrane separation, adsorption, reduction, electrodialysis, and chemical precipitation [35–42]. Compared with the above procedures, the photocatalytic reduction has been considered as a low-cost technique with the merits of the low energy consumption and non-secondary pollution [43]. BiOX (X = Cl, Br, I) photocatalysts have been the comprehensive application in the degradation of organic dyes and pollutants, and recently, it is proved that BiOX photocatalysts also display great potential to the photoreduction of Cr(VI) ions [44–52]. However, these obtained BiOX materials have poor ability to photoreduce Cr(VI) ions.

Herein, few-layer BiOBr nanosheets with oxygen vacancies have been designed and fabricated by solvothermal reaction using ethylene glycol as a solvent. The photocatalytic activity of the as-made products was assessed by photoreduction of Cr(VI) under the visible light irradiation. The obtained BiOBr-Ov displays superior photocatalytic performance with a complete reduction of Cr(VI) (20 mg/L) within 12 and 14 min at acid and neutral condition, respectively. The enhancement on the photocatalytic activity could be attributed to the presence of oxygen vacancies, which can narrow band gap, effectively trap photoelectrons at the oxygen vacancy sites, and suppress the photogenerated electron-hole recombination.

## 2. Results and Discussion

BiOBr samples have been synthesized by a simple solvothermal reaction, and their XRD patterns were shown in Figure 1. It can be found that the main diffraction peaks of as-synthesized BiOBr are all indexed to tetragonal crystal phase (JCPDS No. 09-0393) [53]. Furthermore, no other diffraction peaks are detected, indicative of the high purity and single-phase of as-made samples. The intensity of (001) peaks in BiOBr is the strongest among all the diffraction peaks, indicating that the as-made sample exposes (001) crystal facets. However, all the (00L) related planes (L = 1, 2, 3 and 4) in BiOBr-Ov obtained from the ethylene glycol/water solvent suffer from serious weakened intensity. Therefore, it's believed that the possible reason accounting for the reduced (00L) peaks arises from defects on the (001) facets that seriously deteriorate the diffraction of X-ray on such facets [54].

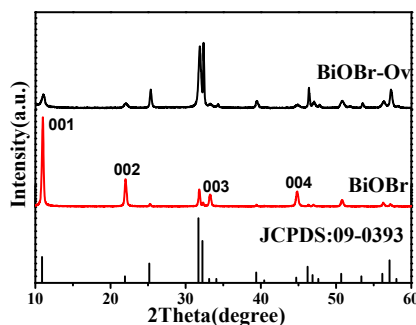


**Figure 1.** The XRD patterns of the obtained BiOBr and BiOBr-Ov.

The FESEM images of the obtained BiOBr were shown in Figure S1. It can be found that the obtained BiOBr and BiOBr-Ov are all ultrathin nanosheets. Figure 2a,c shows the atomic force microscopy (AFM) images of BiOBr-Ov and BiOBr. Cross-sectional line profiles of them are illustrated in Figure 2b,d. It can be seen that the thickness of the obtained BiOBr-Ov and BiOBr nanosheet is 1.238 and 3.168 nm, respectively. Fifty nanosheets were measured, and their thickness is in the range of 1.1–1.5 and 3.0–3.5 nm. The thickness of a single unit cell (atomic layer) along the [001] orientation is 0.818 nm for BiOBr with tetragonal crystal phase. AFM results confirm that BiOBr-Ov with two-layers, and BiOBr with four-layers were successfully synthesized.

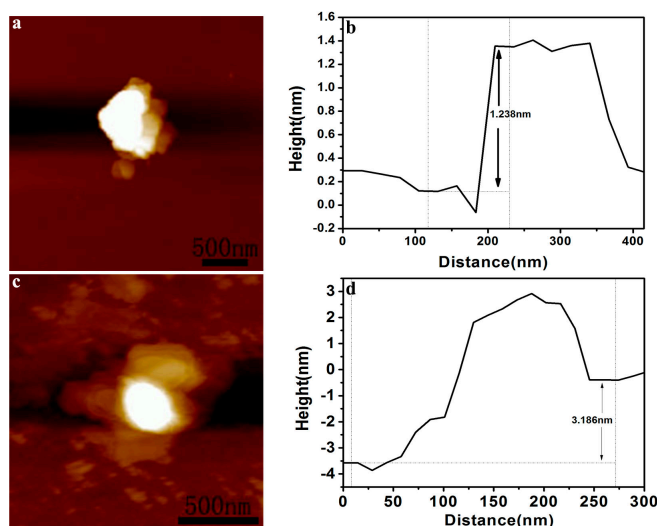


**Figure 2.** Atomic force microscopy (AFM) images of BiOBr-Ov (a) and BiOBr (c); cross-sectional line profiles of BiOBr-Ov (b) and BiOBr (d).

TEM image (Figure 3a) of BiOBr shows that BiOBr is a few-layer nanosheet. The clear lattice fringes with a distance of ca. 0.277 nm (Figure 3b) is indexed to the (110) crystal plane. Meanwhile, the selected area electron diffraction (SAED) pattern of the BiOBr nanosheet (inset in Figure 3b) gives a paralleled spot pattern, which shows the single crystal structure. Two nearest spots with the angle of  $45^\circ$  are ascribed to the (200) and (110) planes, proving that the BiOBr ultrathin nanosheets mainly expose the (001) facet. The lattice fringes and SAED pattern of BiOBr-Ov are all the same with that of BiOBr, which indicates that BiOBr-Ov also mainly exposes (001) crystal facets. Interestingly, some streaky or stretched spots indexed to defect sites can be observed in the SAED pattern of BiOBr-Ov (see red arrows in Figure 3d) [55,56]. So, some defects are formed in BiOBr-Ov using ethylene glycol/water as a solvent. During solvothermal synthesis, ethylene glycol molecules can extract lattice oxygen atoms and leave oxygen vacancies on the (001) crystal facets of BiOBr [54].

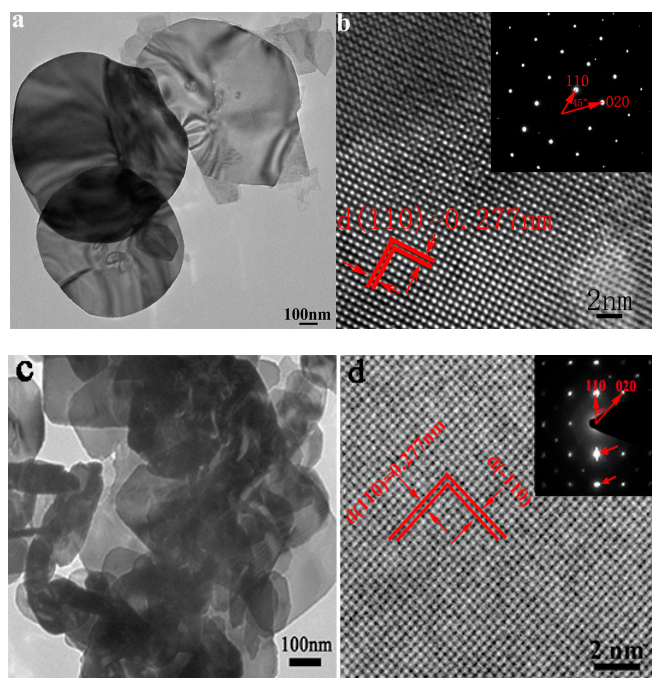


**Figure 3.** TEM (a,c) and high-resolution TEM (HRTEM) (b,d) images of the obtained samples. BiOBr (a,b); BiOBr-Ov (c,d).

In order to prove the presence of oxygen defects in the BiOBr-Ov sample, electron paramagnetic resonance (EPR) spectroscopy, which could be regarded as an effective technique to present direct evidence of oxygen vacancies is measured. As shown in Figure 4, a strong EPR signal at about  $g = 2.004$  can be found for the BiOBr-Ov sample, indicating oxygen vacancies existence [57]. However, no obvious EPR signal for BiOBr appears which proves no oxygen vacancies exist in BiOBr sample.

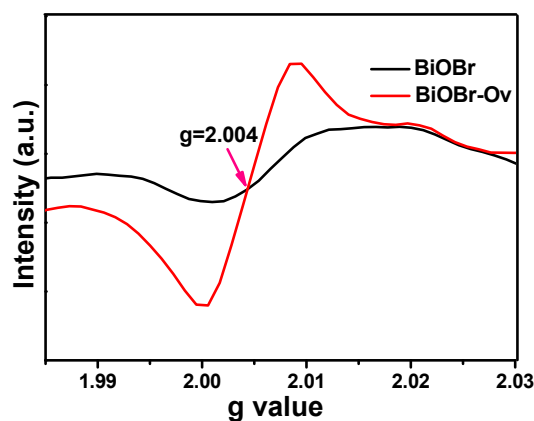


**Figure 4.** Electron paramagnetic resonance (EPR) spectrum of the obtained samples.

The compositions of BiOBr and BiOBr-Ov samples were further investigated by XPS. It can be found from Figure 5a that the signals of Bi, C, O and Br are clearly detected. Figure 5b shows the high-resolution XPS spectra for the O1s. The binding energies at 530.28 eV are attributed to the Bi–O bond in the BiOBr sample. In addition to the Bi–O bond, there is a unique peak observed at 531.53 eV, which is ascribed to the vacancy oxygen [58,59]. Compared with the BiOBr, the intensity of the peak assigned to the vacancy oxygen at 531.56 eV is much stronger in BiOBr-Ov, indicative of more vacancy oxygen in BiOBr-Ov. The peaks located at 159.92 eV and 164.25 eV are ascribed to Bi 4f<sub>7/2</sub> and Bi 4f<sub>5/2</sub>, respectively (Figure 5c), indicating the existence of Bi<sup>3+</sup> in the BiOBr sample. It should be pointed out that the peaks of Bi 4f for the BiOBr-Ov shift at ~0.1 eV toward lower binding energy in comparison

with BiOBr, strongly proves the appearance of  $\text{Bi}^{(3-x)+}$  due to the formation of neighboring oxygen vacancies with a high electron-attracting effect [26]. A similar phenomenon is also found in the XPS spectra of Br 3d (Figure 5d) and O1s, which results from the removal of oxygen atoms bonded with Bi atoms.

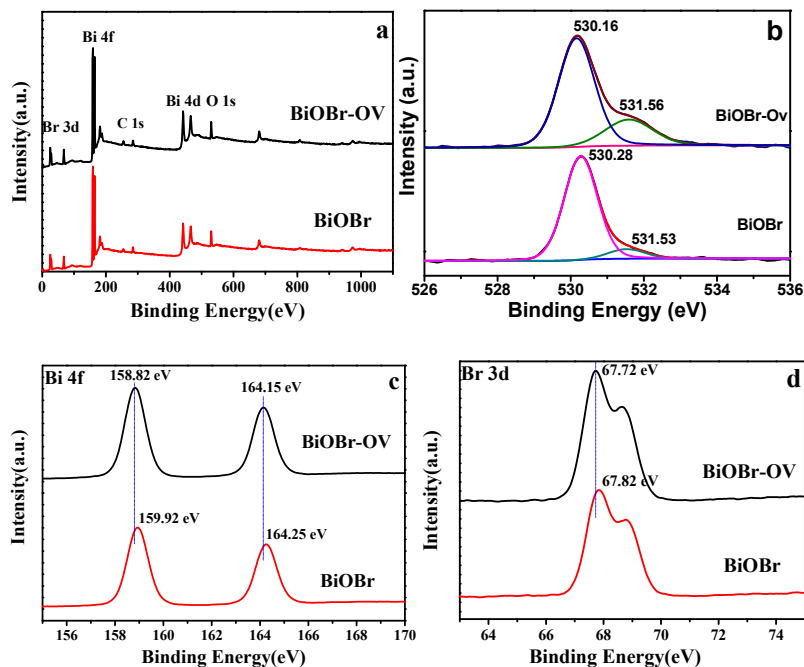


**Figure 5.** (a) Survey X-ray photoelectron spectroscopy (XPS) spectra and high-resolution XPS spectra of (b) O 1s, (c) Bi 4f and (d) Br 3d for BiOBr and BiOBr-OV sample.

$\text{N}_2$  Nitrogen adsorption–desorption isotherms and pore-size distributions of the BiOBr-Ov and BiOBr samples are shown in Figure 6. It can be calculated that the BET surface areas of the BiOBr and BiOBr-Ov are  $7.23$  and  $10.84 \text{ m}^2 \cdot \text{g}^{-1}$ , respectively. The larger BET surface area of BiOBr-Ov can improve its photocatalytic activity. The pore size distribution curves (Figure 6b) show that no pores exist in both BiOBr and BiOBr-Ov.

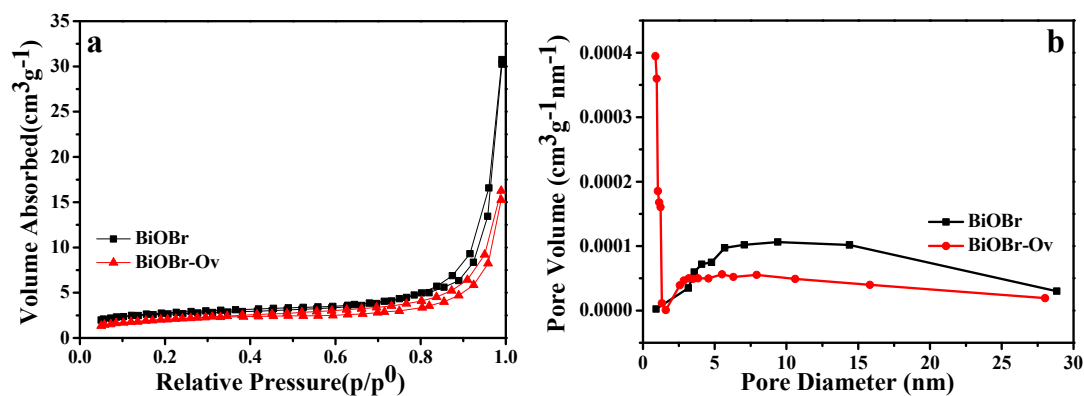


**Figure 6.** (a) Nitrogen adsorption–desorption isotherms and (b) the corresponding pore-size distributions of BiOBr and BiOBr-Ov.

Cr(VI) has been regarded as one of the most harmful metals in all heavy metals which destroy the environment through different industrial paths. A long-term exposure of Cr(VI) would be fatal to living organisms. As a result, it is highly desirable to exploit efficient catalyst to reduce Cr(VI) in wastewater to Cr(III). It is found that BiOBr-Ov presents better reduction efficiency than BiOBr at

acid or neutral condition (Figure 7a–d), and 20 mg/L of Cr(VI) can be completely photoreduced by BiOBr-Ov within 40 and 12 min at neutral and acid condition, respectively. The photocatalytic activity of BiOBr-Ov for the Cr(VI) reduction is higher than most of other recently reported photocatalysts (Table 1). The recycling experiments over the BiOBr-Ov exhibit slight loss over five cycles (Figure 7e). From the XRD pattern and SEM image (Figure 7f,g), it can be found that the BiOBr-Ov exhibits good photostability. Interestingly, Cr(VI) with high concentration (30 mg/L) can be photoreduced by BiOBr-Ov in 2 min under solar light irradiation at acid condition (Figure S2a). Compared with other reported photocatalysts, BiOBr-Ov displays outstanding ability for Cr(VI) reduction [52]. The recycling experiments over the BiOBr-Ov also show some loss over five cycles (Figure S2b). The reason for the decreased activity is ascribed to the formation of a large number of photocatalytic reduction products (Cr(III)) in a short time, which cover on the surface active sites of BiOBr-Ov. The photocatalytic activities of the as-synthesized samples were also evaluated by degrading MO under visible/solar light irradiation (Figure S3). The BiOBr-Ov possesses the better photocatalytic performance than BiOBr, and 100% of MO can be completely degraded in a short time under the visible/solar light irradiation.

**Table 1.** Brief summary of recently reported materials for photocatalytic Cr(VI) reduction under visible light irradiation.

No.	Material	Reaction Condition			Time (min)	Reduction Rate (%)	Ref.
		Catalyst (mg)	Volume (mL)	Cr(VI) (mg/L)			
1	Conjugated polyelectrolyte photocatalyst (P-FL-BT-3)	1	5	25	120	100	[60]
2	BiVO <sub>4</sub> /Bi <sub>2</sub> S <sub>3</sub>	10	20	10	60	92	[61]
3	Metal–organic framework (NH <sub>2</sub> -MIL-88B (Fe))	20	40	8	40	100	[62]
4	R-TiO <sub>2</sub> :N	25	100	10	10	100	[63]
5	Bi <sub>24</sub> O <sub>31</sub> Br <sub>10</sub>	50	50	50	40	100	[47]
6	Carbon dots coupled TiO <sub>2</sub> mesocrystals	20	20	10	20	100	[64]
7	Bi <sub>4</sub> O <sub>5</sub> Br <sub>x</sub> I <sub>2-x</sub> solid solutions	20	50	60	60	100	[48]
8	P doped-g-C <sub>3</sub> N <sub>4</sub>	50	50	20	60	100	[65]
<b>9</b>	<b>BiOBr-Ov</b>	<b>40</b>	<b>40</b>	<b>20</b>	<b>12</b>	<b>100</b>	<b>Our work</b>

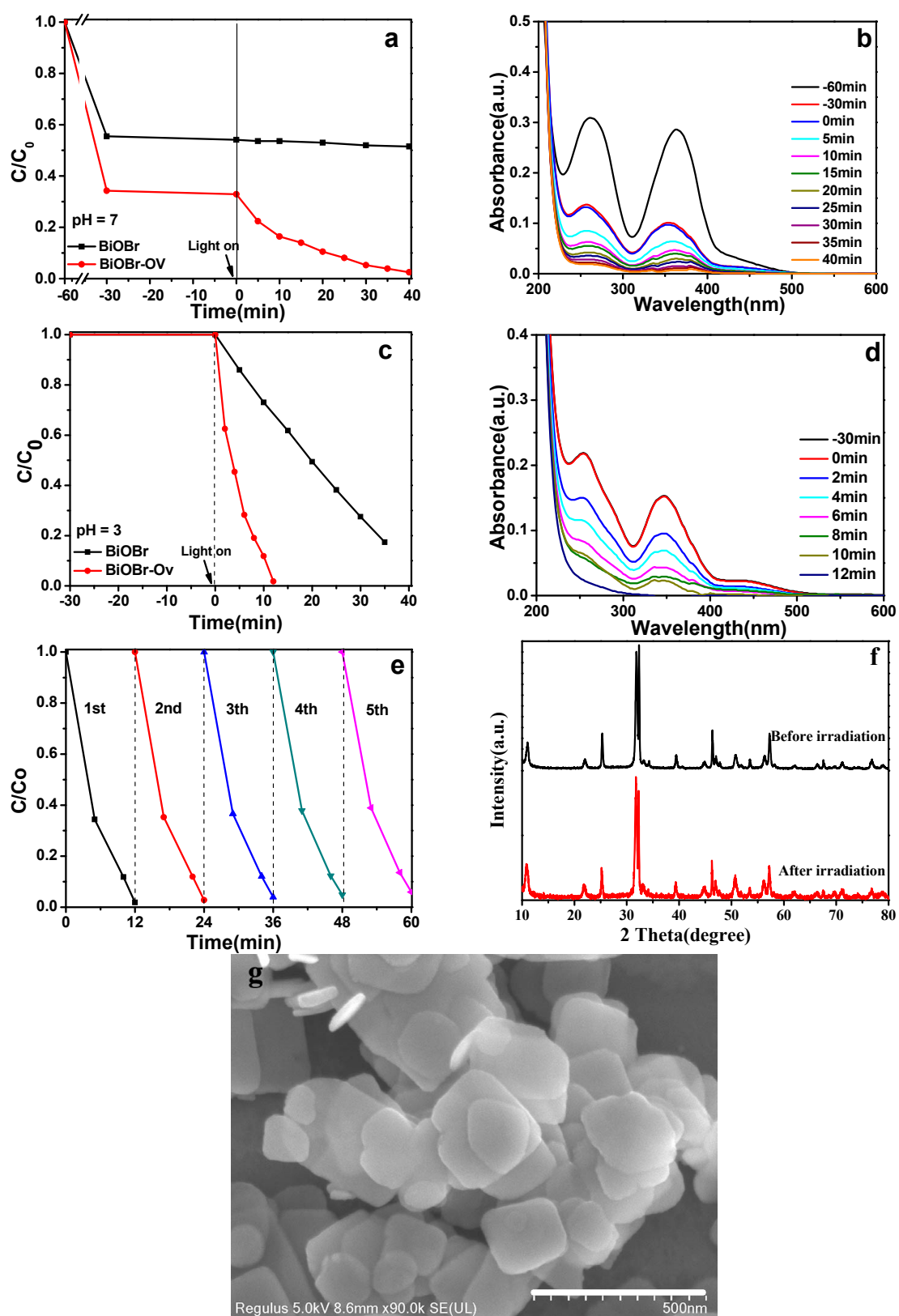


**Figure 7.** (a,c) Photocatalytic activity for reduction of Cr(VI) (20 mg/L) under visible light irradiation at pH = 7 and pH = 3, (b,d) UV-Vis absorbance spectrum of Cr(VI); (e) cycling times of the photoreduction of Cr(VI); (f) XRD patterns of BiOBr-Ov before and after five cycles, and SEM image (g) of the BiOBr-Ov after five cycles.

The optical absorption properties of BiOBr-Ov and pure BiOBr samples were investigated by the UV-vis DRS. It can be seen that pure BiOBr has absorption in the visible light range with an absorption edge at around 420 nm. BiOBr-Ov exhibits slighter red-shifts and the absorption edge is at 427 nm (Figure 8a), demonstrating that oxygen vacancies can effectively narrow the band gap of semiconductor and expand absorptive range. Furthermore, the optical band gap of BiOBr and BiOBr-Ov can be calculated by the following Equation (1) [66]:

$$\alpha h\nu = A(h\nu - E_g)^{n/2} \quad (1)$$

where  $\alpha$ ,  $h$ ,  $\nu$ ,  $A$  and  $E_g$  are the absorption coefficient, Planck constant, light frequency, a constant and band gap, respectively. And  $n$  equals to 4 and 1 for indirect band gap and direct band gap, respectively. Here  $n = 4$  for BiOBr. Figure 8b gives out the plots of  $(\alpha h\nu)^{1/2}$  compared to  $h\nu$  of BiOBr and BiOBr-Ov. The band gap ( $E_g$ ) is estimated by extrapolating the straight line to the abscissa axis. So,  $E_g$  (BiOBr) and  $E_g$  (BiOBr-Ov) are deduced to be 2.84 and 2.76 eV. The band gap energy of BiOBr-Ov is obviously lower than that of BiOBr, which might be attributed to the overlapping of the band edge of the semiconductor and surface defect electronic states with a high concentration of oxygen vacancies [54]. Valence band X-ray photoelectron spectroscopy (VB-XPS) for BiOBr and BiOBr-Ov were surveyed to determine the relative positions of the conduction band (CB) and valence band (VB) edges. It can be clearly seen from Figure 8c that the  $E_{VB}$  top of BiOBr and BiOBr-Ov are located at 1.45 and 1.30 eV, respectively. According to the VB edges of BiOBr and BiOBr-Ov, and combined with the band gap derived from DRS, the CB edge potentials of the two semiconductors can thus be obtained by the equation of  $E_{CB} = E_{VB} - E_g$ . The conduction band (CB) edge potentials of BiOBr and BiOBr-Ov are estimated at  $-1.39$  eV and  $-1.46$  eV, respectively.

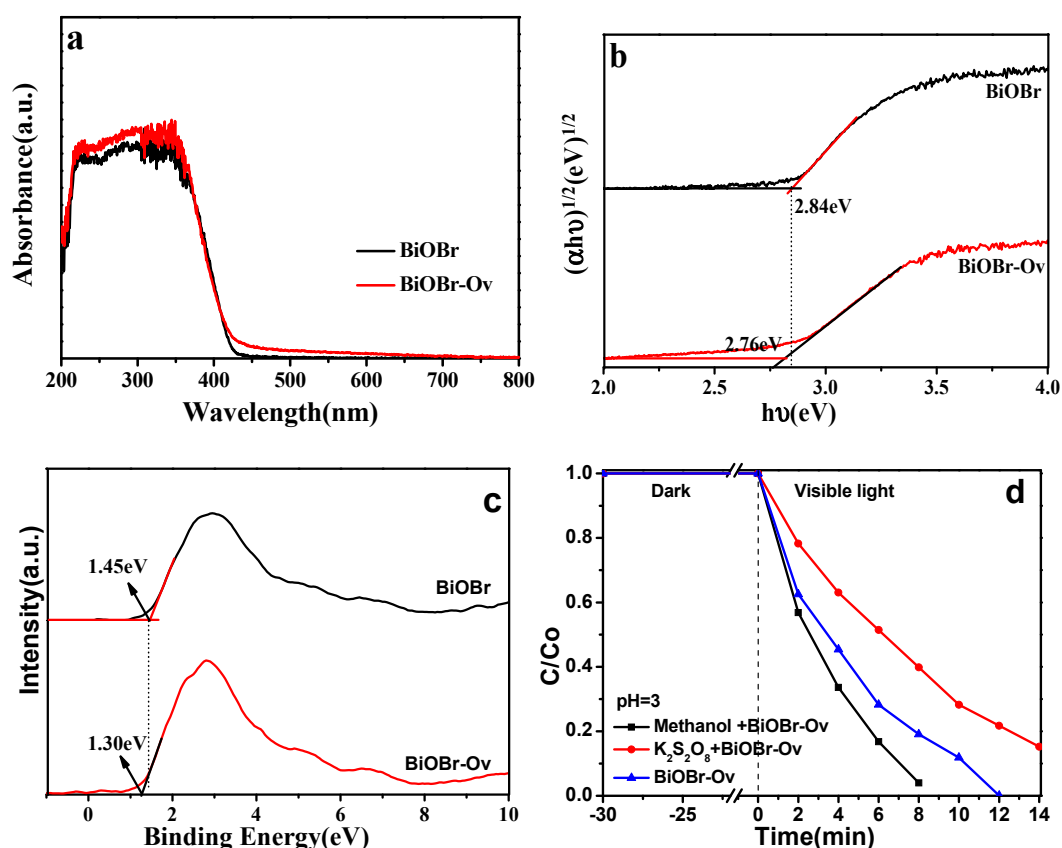


**Figure 8.** (a) UV-Vis diffuse reflectance spectra, (b) the plots of  $(\alpha h\nu)^{1/2}$  vs.  $h\nu$  and (c) valence band X-ray photoelectron spectroscopy (VB-XPS) spectra of BiOBr and BiOBr-Ov, (d) photogenerated carriers trapping for photoreduction of Cr(VI).

To further investigate the photocatalytic mechanism and to clarify the roles of different reactive species ( $h^+$  and  $e^-$ ), different scavengers were added during the photocatalytic process. Trapping of electrons and holes were performed using  $K_2S_2O_8$  and methanol as electrons and  $h^+$  scavengers, respectively. As shown in Figure 8d, the photoreduction activity of Cr(VI) for BiOBr-Ov decreases significantly when the electron trapping agent ( $K_2S_2O_8$ ) is added, indicating the electrons are the main active species and directly participate in the Cr(VI) photoreduction reaction. However, the addition of methanol increases obviously the photoreduction efficiency of Cr(VI), which indicates that trapping  $h^+$  will make more photogenerated electrons involve in the photoreducing Cr(VI) reaction.

According to UV-vis DRS, VB-XPS and trapping experiment analysis, the schematic photocatalytic mechanism for the reduction of Cr(VI) is shown in Figure 9. It can be found that the VB potential (1.45 eV) of BiOBr and BiOBr-Ov (1.30 eV) is all enough positive to  $E^0$  ( $Cr_2O_7^{2-}/Cr^{3+}$ ) (1.23 eV compared to NHE), which shows that the photogenerated holes of BiOBr or BiOBr-Ov can't reduce Cr(VI) to Cr(III) during photocatalysis. However, the CB potential of BiOBr (-1.39 eV) or BiOBr-Ov (-1.46 eV) is all lower than that of  $E^0$  ( $Cr_2O_7^{2-}/Cr^{3+}$ ), which indicates that the photogenerated electrons can directly reduce Cr(VI) ions adsorbed on the surface of the BiOBr or BiOBr-Ov to Cr(III) ions, which is consistent with the result of the trapping experiment. A new energy level is formed in the band gap due to the existence of oxygen defects in the BiOBr-Ov sample. So, more photogenerated electrons are provided to take part in the photoreduction of Cr(VI), which makes the BiOBr-Ov display high photoreduction ability.

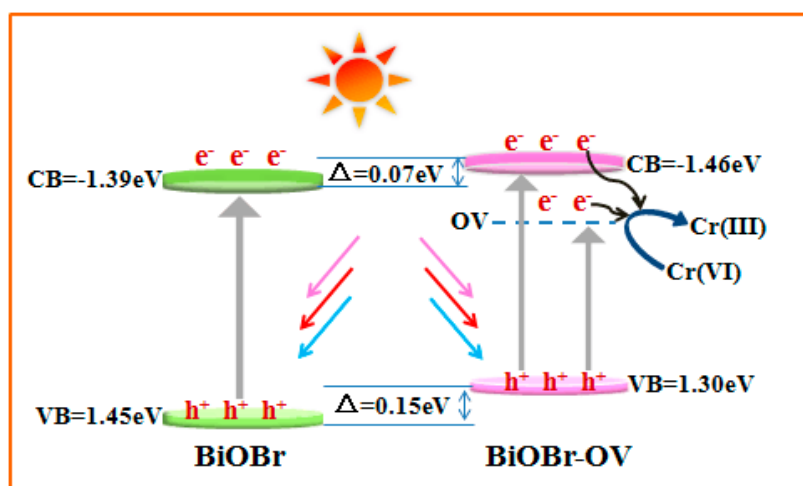


Figure 9. Schematic representation of photoreduction mechanism for Cr(VI).

To prove this viewpoint, the electrochemical impedance and photocurrent of the obtained samples, which are the effective strategies to check the amount of photogenerated charge carriers, were performed. As shown in Figure 10a, it can be clearly found that the photocurrent intensities of BiOBr-Ov is obviously higher than that of BiOBr, which shows that much photogenerated electrons are produced in BiOBr-Ov than in BiOBr. The electrochemical impedance test further confirms these results (Figure 10b) because BiOBr-Ov gives a lower slope than BiOBr. So it can be concluded that oxygen vacancies in BiOBr-Ov play the key role in improving the separation efficiency of photogenerated charge carrier.

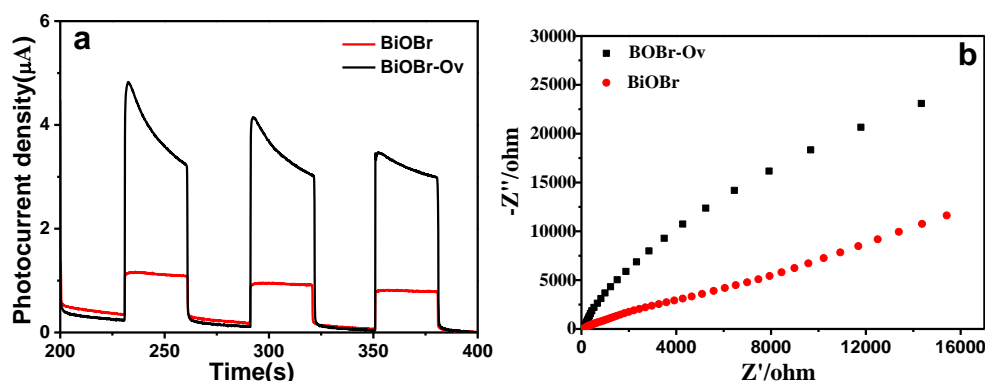


Figure 10. (a) Electrochemical impedance spectra and (b) photocurrent of BiOBr and BiOBr-Ov.

### 3. Experimental Section

#### 3.1. Photocatalyst Synthesis

All the reagents utilized in the experiments were analytical grade and used without further purification.

In the typical synthesis, 2 mmol  $\text{Bi}(\text{NO}_3)_3 \cdot 5\text{H}_2\text{O}$  (Guo Yao chemical company, Nanjing, China) was dissolved in 15 mL  $\text{H}_2\text{O}$  (or 15 mL ethylene glycol) solution (solution A), and 2 mmol cetyltriethylammonium bromide (CTAB) (Guo Yao chemical company, Nanjing, China) was dissolved in 15 mL  $\text{H}_2\text{O}$  solution (solution B). Solution A was added into solution B with vigorous magnetically stirring for 1 h. Then, the above mixture was introduced into a Teflon-lined autoclave, maintaining at 453 K for 24 h. The resulting solids were rinsed with deionized water and ethanol several times. Then, the obtained products were finally dried in the oven at 333 K for 4 h. The samples obtained from  $\text{H}_2\text{O}$  and  $\text{H}_2\text{O}$ /ethylene glycol solvents were denoted as BiOBr and BiOBr-Ov, respectively.

#### 3.2. Photocatalytic Activity Assessment

The photocatalytic activity of the as-prepared BiOBr samples was determined by detoxifying heavy metal ion Cr(VI) with the condition of visible/solar light irradiation. A 300 W Xe lamp (CEL-HXF300F, Beijing China Education Au-light Co., Ltd., Beijing, China) with a cut-off filter at 400 nm was served as a visible light source. In a typical experiment, the photocatalyst (40 mg) was added into 40 mL  $\text{K}_2\text{Cr}_2\text{O}_7$  (or methyl orange (MO)) solution (Guo Yao chemical company, Nanjing, China). The mixture was ultrasonicated for 10 min to form a suspension for the degradation reaction. Before irradiation, the suspension was magnetically stirred for 30 min in the dark to achieve the Cr(VI) species (or MO molecules) adsorption/desorption equilibrium on the surface of the catalyst. After that, the suspension was illuminated by solar/visible light under magnetic stirring. By extracting a 4 mL aliquot from the reaction mixture and making centrifugation to remove the precipitate, UV-Vis spectroscopy was periodically monitored to obtain the Cr(VI) (or MO) concentration as a function of irradiation time.

#### 3.3. Electrochemical Impedance Spectroscopy (EIS) and Photoelectrochemical Measurements

Electrochemical impedance spectroscopy (EIS) measurements were performed at a frequency between 0.1 Hz and 100 kHz using a CHI660D instrument (Shanghai Chenhua Limited, Shanghai, China). A three-electrode electrochemical setup was applied, where the counter electrode and reference electrode were used with a platinum wire and saturated calomel, respectively. Working electrodes were constructed by a BiOBr and BiOBr-Ov film on ITO, separately. The  $[\text{Fe}(\text{CN})_6]^{3-/4-}$  solution containing 10 mM  $\text{K}_3\text{Fe}(\text{CN})_6$ , 10 mM  $\text{K}_4\text{Fe}(\text{CN})_6$  and 0.1 M KCl (as the supporting electrolyte) was prepared as the detecting electrolyte.

Photoelectrochemical test systems were composed of a CHI 660D electrochemistry potentiostat (Shanghai Chenhua Limited, China), a 300 W xenon lamp with cutoff filters ( $\lambda \geq 400$  nm), and a

homemade three-electrode cell with using Pt wire as the counter electrode and Ag/AgCl as the reference electrode, and 1 M Na<sub>2</sub>SO<sub>4</sub> as the electrolyte. BiOBr and BiOBr-Ov electrodes were prepared by depositing suspensions (the concentration of sample dissolved by absolute ethanol is 10 mg·mL<sup>-1</sup>) onto Ti foil using the doctor-blade coating method with a glass rod and scotch tape as a frame and spacer, respectively. The electrodes were annealed at 90 °C for 24 h. During measurements, the electrodes were pressed against a □-shape of an electrochemical cell with a working area of 4.0 cm<sup>2</sup>.

### 3.4. Characterization

X-ray powder diffraction (XRD) pattern was collected on a Rigaku D/max-γA X-ray diffractometer using Cu-Kα radiation (λ = 0.154178 nm). Scanning electron microscopy (SEM) images were performed on a Hitachi S-4800 microscope. High-resolution transmission electron microscopic (HRTEM) images were obtained by a JEOL-ARM200F microscope with an accelerating voltage of 200 kV. The UV-vis diffuse-reflectance spectra were surveyed with a UV-2450 spectrophotometer in the wavelength range from 200 to 800 nm at room temperature, with BaSO<sub>4</sub> as the reflectance standard material. The X-ray photoelectron spectroscopy (XPS) was performed on a Perkin-Elmer RBD upgraded PHI-5000C ESCA system. The electron paramagnetic resonance (EPR) spectra were recorded on a Bruker (A200-9.5/12) spectrometer with the X-band frequency of 9.8 GHz under room temperature. Nitrogen adsorption–desorption measurements were performed at 77 K using a Micromeritics Tristar II 3020 M analyzer after the samples were degassed at 180 °C for 6 h. The Brunauer–Emmett–Teller (BET) surface area was estimated by using adsorption data in a relative pressure range of 0.05 to 0.3. The thickness of the BiOBr and BiOBr-Ov nanosheets was determined by AFM measurement (SPA-300HV&SPI3800N).

## 4. Conclusions

In brief, few-layer BiOBr nanosheets with oxygen vacancies (BiOBr-Ov) have been prepared via a simple solvothermal reaction with the help of ethylene glycol. The existence of oxygen vacancies in the BiOBr-Ov sample have been verified by the techniques of HRTEM, XPS and ESR. The obtained BiOBr-Ov displays superior photocatalytic performance, with a complete reduction of Cr(VI) (20 mg/L) within 12 and 40 min at acid and neutral condition, respectively. This enhancement on the photocatalytic performance could be contributed to the existence of oxygen vacancies which can narrow band gap, trap electrons and suppress recombination of photogenerated electrons and holes. The large BET surface area maybe is a reason to enhance the photocatalytic activity.

**Supplementary Materials:** The following are available online at <http://www.mdpi.com/2073-4344/9/6/558/>, Figure S1: SEM images of the obtained BiOBr (a) and BiOBr-Ov (b) samples, Figure S2: (a) The photocatalytic reduction curve of Cr(VI) (30 mg/L) and (b) Cycling times of the photoreduction of Cr(VI) under solar light irradiation, Figure S3: (a,c) The Photocatalytic degradation curve of MO (10 mg/L), and (b,d) UV–Vis absorption spectra of MO (10 mg/L) using BiOBr-OV as photocatalyst under visible/solar light irradiation.

**Author Contributions:** Y.P. conceived and designed the experiments; P.K. performed the experiments; P.K. and Q.Z. analyzed the data; Y.P. wrote the paper and Y.Z. revised the paper.

**Funding:** This work is supported by the National Natural Science Foundation of China (No. 21771004) and the fund of state key laboratory of physical chemistry of solid surfaces, Xiamen University (201510).

**Conflicts of Interest:** The authors declare no conflict of interest.

## References

1. Xiang, Q.J.; Cheng, B.; Yu, J.G. Graphene-based photocatalysts for solar-fuel generation. *Angew. Chem. Int. Ed.* **2015**, *54*, 11350–11366. [[CrossRef](#)] [[PubMed](#)]
2. Jin, X.; Ye, L.; Xie, H.; Chen, G. Bismuth-rich bismuth oxyhalides for environmental and energy photocatalysis. *Coord. Chem. Rev.* **2017**, *349*, 84–101. [[CrossRef](#)]
3. Ma, Y.; Wang, X.; Jia, Y.; Chen, X.; Han, H.; Li, C. Titanium dioxide-based nanomaterials for photocatalytic fuel generations. *Chem. Rev.* **2014**, *114*, 9987–10043. [[CrossRef](#)] [[PubMed](#)]

4. Kou, J.; Lu, C.; Wang, J.; Chen, Y.; Xu, Z.; Varma, R.S. Selectivity Enhancement in Heterogeneous Photocatalytic Transformations. *Chem. Rev.* **2017**, *117*, 1445–1514. [[CrossRef](#)] [[PubMed](#)]
5. Kudo, A.; Miseki, Y. Heterogeneous photocatalyst materials for water splitting. *Chem. Rev.* **2009**, *38*, 253–278. [[CrossRef](#)]
6. Li, J.; Cai, L.; Shang, J.; Yu, Y.; Zhang, L. Giant enhancement of internal electric field boosting bulk charge separation for photocatalysis. *Adv. Mater.* **2016**, *28*, 4059–4064. [[CrossRef](#)] [[PubMed](#)]
7. Ghosh, M.; Liu, J.; Chuang, S.S.C.; Jana, S.C. Fabrication of hierarchical V<sub>2</sub>O<sub>5</sub> nanorods on TiO<sub>2</sub> nanofibers and their enhanced photocatalytic activity under visible light. *ChemCatChem* **2018**, *10*, 3305–3318. [[CrossRef](#)]
8. Liu, G.; Yang, H.G.; Pan, J.; Yang, Y.Q.; Lu, G.Q.; Cheng, H.-M. Titanium dioxide crystals with tailored facets. *Chem. Rev.* **2014**, *114*, 9559–9612. [[CrossRef](#)]
9. Peng, Y.; Wang, K.K.; Liu, T.; Xu, J.; Xu, B. Synthesis of one-dimensional Bi<sub>2</sub>O<sub>3</sub>-Bi<sub>2</sub>O<sub>2.33</sub> heterojunctions with high interface quality for enhanced visible light photocatalysis in degradation of high-concentration phenol and MO dyes. *Appl. Catal. B-Environ.* **2017**, *203*, 946–954. [[CrossRef](#)]
10. Wang, J.; Wang, Z.; Huang, B.; Ma, Y.; Liu, Y.; Qin, X.; Zhang, X.; Dai, Y. Oxygen vacancy induced band-gap narrowing and enhanced visible light photocatalytic activity of ZnO. *ACS Appl. Mater. Interf.* **2012**, *4*, 4024–4030. [[CrossRef](#)]
11. Peng, Y.; Yan, M.; Chen, Q.G.; Fan, C.M.; Zhou, H.Y.; Xu, A.W. Novel onedimensional Bi<sub>2</sub>O<sub>3</sub>-Bi<sub>2</sub>WO<sub>6</sub> p-n hierarchical heterojunction with enhanced photocatalytic activity. *J. Mater. Chem. A* **2014**, *2*, 8517–8524. [[CrossRef](#)]
12. Mi, Y.; Li, H.; Zhang, Y.; Du, N.; Hou, W. Synthesis and photocatalytic activity of BiOBr nanosheets with tunable crystal facets and sizes. *Catal. Sci. Technol.* **2018**, *8*, 2588–2597. [[CrossRef](#)]
13. Wang, H.; Yong, D.; Chen, S.; Jiang, S.; Zhang, X.; Shao, W.; Zhang, Q.; Yan, W.; Pan, B.; Xie, Y. Oxygen-vacancy-mediated exciton dissociation in BiOBr for boosting charge-carrier-involved Molecular oxygen activation. *J. Am. Chem. Soc.* **2018**, *140*, 1760–1766. [[CrossRef](#)] [[PubMed](#)]
14. Tan, C.; Cao, X.; Wu, X.-J.; He, Q.; Yang, J.; Zhang, X.; Chen, J.; Zhao, W.; Han, S.; Nam, G.-H.; et al. Recent advances in ultrathin two-dimensional nanomaterials. *Chem. Rev.* **2017**, *117*, 6225–6331. [[CrossRef](#)] [[PubMed](#)]
15. Yin, H.; Tang, Z. Ultrathin two-dimensional layered metal hydroxides: An emerging platform for advanced catalysis, energy conversion and storage. *Chem. Soc. Rev.* **2016**, *45*, 4873–4891. [[CrossRef](#)] [[PubMed](#)]
16. Deng, D.; Novoselov, K.S.; Fu, Q.; Zheng, N.; Tian, Z.; Bao, X. Catalysis with two-dimensional materials and their heterostructures. *Nat. Nanotechnol.* **2016**, *11*, 218. [[CrossRef](#)] [[PubMed](#)]
17. Nasilowski, M.; Mahler, B.; Lhuillier, E.; Ithurria, S.; Dubertret, B. Two-Dimensional Colloidal Nanocrystals. *Chem. Rev.* **2016**, *116*, 10934–10982. [[CrossRef](#)]
18. Gao, S.; Gu, B.; Jiao, X.; Sun, Y.; Zu, X.; Yang, F.; Zhu, W.; Wang, C.; Feng, Z.; Ye, B.; et al. Highly efficient and exceptionally durable CO<sub>2</sub> photoreduction to methanol over freestanding defective single-unit-cell bismuth vanadate layers. *J. Am. Chem. Soc.* **2017**, *139*, 3438–3445. [[CrossRef](#)]
19. Di, J.; Xia, J.; Li, H.; Liu, Z. Freestanding atomically-thin two-dimensional materials beyond graphene meeting photocatalysis: Opportunities and challenges. *Nano Energy* **2017**, *35*, 79–91. [[CrossRef](#)]
20. Sun, Y.; Gao, S.; Lei, F.; Xie, Y. Atomically-thin two-dimensional sheets for understanding active sites in catalysis. *Chem. Soc. Rev.* **2015**, *44*, 623–636. [[CrossRef](#)]
21. Liu, Y.; Xiao, C.; Li, Z.; Xie, Y. Vacancy engineering for tuning electron and phonon structures of two-dimensional materials. *Adv. Energy Mater.* **2016**, *6*, 1600436. [[CrossRef](#)]
22. Li, X.D.; Shi, W.; Ling, P.Q.; Sun, Y.F.; Jiao, X.C.; Gao, S.; Liang, L.; Xu, J.Q.; Yan, W.S.; Wang, C.M.; et al. Efficient visible-light-driven CO<sub>2</sub> reduction mediated by defect-engineered BiOBr atomic layers. *Angew. Chem. Int. Ed.* **2018**, *130*, 8855–8859. [[CrossRef](#)]
23. Lei, F.; Sun, Y.; Liu, K.; Gao, S.; Liang, L.; Pan, B.; Xie, Y. Oxygen vacancies confined in ultrathin indium oxide porous sheets for promoted visible-light water splitting. *J. Am. Chem. Soc.* **2014**, *136*, 6826–6829. [[CrossRef](#)] [[PubMed](#)]
24. Li, H.; Shang, J.; Ai, Z.H.; Zhang, L.Z. Efficient visible light nitrogen fixation with BiOBr nanosheets of oxygen vacancies on the exposed {001} facets. *J. Am. Chem. Soc.* **2015**, *137*, 6393–6399. [[CrossRef](#)] [[PubMed](#)]
25. Kong, X.Y.; Ng, B.J.; Tan, K.H.; Chen, X.F.; Wang, H.T.; Mohamed, A.R.; Chai, S.P. Simultaneous generation of oxygen vacancies on ultrathin BiOBr nanosheets during visible-light-driven CO<sub>2</sub> photoreduction evoked superior activity and long-term stability. *Catal. Today* **2018**, *314*, 20–27. [[CrossRef](#)]

26. Xue, X.; Chen, R.; Chen, H.; Hu, Y.; Ding, Q.; Liu, Z.; Ma, L.; Zhu, G.; Zhang, W.; Yu, Q.; et al. Oxygen Vacancy Engineering Promoted Photocatalytic Ammonia Synthesis on Ultrathin Two-Dimensional Bismuth Oxybromide Nanosheets. *Nano Lett.* **2018**, *18*, 7372–7377. [[CrossRef](#)]
27. Shi, X.; Wang, P.Q.; Wang, L.; Bai, Y.; Xie, H.Q.; Zhou, Y.; Wang, J.A.; Li, Z.J.; Qu, L.B.; Shi, M.J.; et al. Few layered BiOBr with expanded interlayer spacing and oxygen vacancies for efficient decomposition of real oil field produced wastewater. *ACS Sustain. Chem. Eng.* **2018**, *6*, 13739–13746. [[CrossRef](#)]
28. Hua, C.H.; Dong, X.L.; Wang, Y.; Zheng, N.; Ma, H.C.; Zhang, X.F. Bi-modified 3D BiOBr microsphere with oxygen vacancies for efficient visible-light photocatalytic performance. *J. Mater. Sci.* **2019**, *54*, 9397–9413. [[CrossRef](#)]
29. McLean, J.E.; McNeill, L.S.; Edwards, M.; Parks, J.L. Factors controlling micropollutant removal during riverbank filtration. *J. Am. Water Works Assoc.* **2012**, *104*, 35–36.
30. Mishra, S.; Bharagava, R.N. Toxic and genotoxic effects of hexavalent chromium in environment and its bioremediation strategies. *J. Environ. Sci. Health C* **2016**, *34*, 1–32. [[CrossRef](#)]
31. Blowes, D. Tracking hexavalent Cr in groundwater. *Science* **2002**, *295*, 2024. [[CrossRef](#)]
32. Vaiopoulou, E.; Gikas, P. Effects of chromium on activated sludge and on the performance of wastewater treatment plants: A review. *Water Res.* **2012**, *46*, 549–570. [[CrossRef](#)]
33. Costa, M. Potential hazards of hexavalent chromate in our drinking water. *Toxicol. Appl. Pharmacol.* **2003**, *188*, 1–5. [[CrossRef](#)]
34. Hsu, L.C.; Wang, S.L.; Lin, Y.C.; Wang, M.K.; Chiang, P.N.; Liu, J.C.; Kuan, W.H.; Chen, C.C.; Tzou, Y.M. Cr(VI) removal on fungal biomass of neurospora crassa: the importance of dissolved organic carbons derived from the biomass to Cr(VI) reduction. *Environ. Sci. Technol.* **2010**, *44*, 6202–6208. [[CrossRef](#)] [[PubMed](#)]
35. Saravanan, A.; Kumar, P.S.; Yashwanthraj, M. Sequestration of toxic Cr(VI) ions from industrial wastewater using waste biomass: A review. *Desalin Water Treat.* **2017**, *68*, 245–266.
36. Qiu, B.; Xu, C.X.; Sun, D.Z.; Wang, Q.; Gu, H.B.; Zhang, X.; Weeks, B.L.; Hopper, J.; Ho, T.C.; Guo, Z.H.; et al. Polyaniline coating with various substrates for hexavalent chromium removal. *Appl. Surf. Sci.* **2015**, *334*, 7–14. [[CrossRef](#)]
37. Pradhan, D.; Sukla, L.B.; Sawyer, M.; Rahman, P.K.S.M. Recent bioreduction of hexavalent chromium in wastewater treatment: A review. *J. Ind. Eng. Chem.* **2017**, *55*, 1–20. [[CrossRef](#)]
38. Pakade, V.; Chimuka, L. Polymeric sorbents for removal of Cr(VI) from environmental samples. *Pure Appl. Chem.* **2013**, *85*, 2145–2160. [[CrossRef](#)]
39. Jiang, Y.L.; Liu, Z.F.; Zeng, G.M.; Liu, Y.J.; Shao, B.B.; Li, Z.G.; Liu, Y.; Zhang, W.; He, Q.Y. Polyaniline-based adsorbents for removal of hexavalent chromium from aqueous solution: A mini review. *Environ. Sci. Pollut. Res. Int.* **2018**, *25*, 6158–6174. [[CrossRef](#)]
40. Fernandez, P.M.; Vinarta, S.C.; Bernal, A.R.; Cruz, E.L.; Figueroa, L.I.C. Bioremediation strategies for chromium removal: Current research, scale-up approach and future perspectives. *Chemosphere* **2018**, *208*, 139–148. [[CrossRef](#)]
41. Dhal, B.; Thatoi, H.N.; Das, N.N.; Pandey, B.D. Chemical and microbial remediation of hexavalent chromium from contaminated soil and mining/metallurgical solid waste: A review. *J. Hazard. Mater.* **2013**, *250*, 272–291. [[CrossRef](#)]
42. Barrera-Diaz, C.E.; Lugo-Lugo, V.; Bilyeu, B. A review of chemical, electrochemical and biological methods for aqueous Cr(VI) reduction. *J. Hazard. Mater.* **2012**, *223*, 1–12. [[CrossRef](#)] [[PubMed](#)]
43. Wang, C.C.; Du, X.D.; Li, J.; Guo, X.X.; Wang, P.; Zhang, J. Photocatalytic Cr(VI) reduction in metal-organic frameworks: A mini-review. *Appl. Catal. B-Environ.* **2016**, *193*, 198–216. [[CrossRef](#)]
44. Fan, Z.; Zhao, Y.B.; Zhai, W.; Qiu, L.; Li, H.; Hoffman, M.R. Facet-dependent performance of BiOBr for photocatalytic reduction of Cr(VI). *RSC Adv.* **2016**, *6*, 2028–2031. [[CrossRef](#)]
45. Han, J.L.; Zhu, G.Q.; Hojamberdiev, M.; Peng, J.H.; Zhang, X.; Liu, Y.; Ge, B.; Liu, P. Rapid adsorption and photocatalytic activity for Rhodamine B and Cr(VI) by ultrathin BiOI nanosheets with highly exposed {001} facets. *New J. Chem.* **2015**, *39*, 1874–1882. [[CrossRef](#)]
46. Shang, J.; Hao, W.; Lv, X.; Wang, T.; Wang, X.; Du, Y.; Dou, S.; Xie, T.; Wang, D.; Wang, J. Bismuth oxybromide with reasonable photocatalytic reduction activity under visible light. *ACS Catal.* **2014**, *4*, 954–961. [[CrossRef](#)]
47. Bai, Y.; Ye, L.; Chen, T.; Wang, P.; Wang, L.; Shi, X.; Wong, P.K. Synthesis of hierarchical bismuth-rich  $\text{Bi}_4\text{O}_5\text{Br}_x\text{I}_{2-x}$  solid solutions for enhanced photocatalytic activities of  $\text{CO}_2$  conversion and Cr(VI) reduction under visible light. *Appl. Catal. B Environ.* **2017**, *203*, 633–640. [[CrossRef](#)]

48. Li, H.; Zhang, L. Oxygen vacancy induced selective silver deposition on the {001} facets of BiOCl single-crystalline nanosheets for enhanced Cr(VI) and sodium pentachlorophenate removal under visible light. *Nanoscale* **2014**, *6*, 7805–7810. [[CrossRef](#)]
49. Shi, Y.Q.; Xiong, X.Y.; Ding, S.P.; Liu, X.F.; Jiang, Q.Q.; Hu, J.C. In-situ topotactic synthesis and photocatalytic activity of plate-like BiOCl/2D networks Bi<sub>2</sub>S<sub>3</sub> heterostructures. *Appl. Catal. B-Environ.* **2018**, *220*, 570–580. [[CrossRef](#)]
50. Wu, Z.Z.; Jiang, Y.F.; Xiong, X.Y.; Ding, S.P.; Shi, Y.Q.; Liu, X.F.; Liu, Y.; Huang, Z.X.; Hu, J.C. Synthesis and characterization of single-crystalline Bi<sub>19</sub>Cl<sub>3</sub>S<sub>27</sub> nanorods. *Catal. Sci. Technol.* **2017**, *7*, 3464–3468. [[CrossRef](#)]
51. Shi, Y.; Xiong, X.; Ding, S.; Liu, X.; Jiang, Q.; Hu, J. In-situ topotactic synthesis and photocatalytic activity of plate-like BiOCl/2D networks Bi<sub>2</sub>S<sub>3</sub> heterostructures. *Appl. Catal. B Environ.* **2018**, *220*, 570–580. [[CrossRef](#)]
52. Peng, Y.; Mao, Y.G.; Kan, P.F.; Liu, J.Y.; Fang, Z. Controllable synthesis and photoreduction performance towards Cr(vi) of BiOCl microrods with exposed (110) crystal facets. *New J. Chem.* **2018**, *42*, 16911–16918. [[CrossRef](#)]
53. Chen, J.; Guan, M.; Cai, W.; Guo, J.; Xiao, C.; Zhang, G. The dominant {001} facet-dependent enhanced visible-light photoactivity of ultrathin BiOBr nanosheets. *Phys. Chem. Chem. Phys. PCCP* **2014**, *16*, 20909–20914. [[CrossRef](#)] [[PubMed](#)]
54. Li, H.; Shi, J.; Zhao, K.; Zhang, L. Sustainable molecular oxygen activation with oxygen vacancies on the {001} facets of BiOCl nanosheets under solar light. *Nanoscale* **2014**, *6*, 14168–14173. [[CrossRef](#)] [[PubMed](#)]
55. Wu, J.M. TiO<sub>2</sub>/Ti<sub>1-x</sub>Sn<sub>x</sub>O<sub>2</sub> heterojunction nanowires: characterization, formation, and gas sensing performance. *J. Mater. Chem. A* **2011**, *21*, 14048–14055. [[CrossRef](#)]
56. Lee, J.; Ham, S.; Choi, D.; Jang, D.-J. Facile fabrication of porous ZnS nanostructures with a controlled amount of S vacancies for enhanced photocatalytic performances. *Nanoscale* **2018**, *10*, 14254–14263. [[CrossRef](#)] [[PubMed](#)]
57. Janotti, A.; Van de Walle, C.G. Oxygen vacancies in ZnO. *Appl. Phys. Lett.* **2005**, *87*, 122102. [[CrossRef](#)]
58. Gao, S.; Sun, Z.; Liu, W.; Jiao, X.; Zu, X.; Hu, Q.; Sun, Y.; Yao, T.; Zhang, W.; Wei, S.; et al. Atomic layer confined vacancies for atomic-level insights into carbon dioxide electroreduction. *Nat. Commun.* **2017**, *8*, 14503–14511. [[CrossRef](#)]
59. Ye, L.; Zan, L.; Tian, L.; Peng, T.; Zhang, J. The {001} facets-dependent high photoactivity of BiOCl nanosheets. *Chem. Commun.* **2011**, *47*, 6951–6953. [[CrossRef](#)]
60. Ghasimi, S.; Prescher, S.; Wang, Z.J.; Landfester, K.; Yuan, J.; Zhang, K.A.I. Heterophase photocatalysts from water-soluble conjugated polyelectrolytes: an example of self-initiation under visible light. *Angew. Chem. Int. Ed.* **2015**, *54*, 14549–14553. [[CrossRef](#)]
61. Gao, X.; Wu, H.B.; Zheng, L.; Zhong, Y.; Hu, Y.; Lou, X.W. Formation of mesoporous heterostructured BiVO<sub>4</sub>/Bi<sub>2</sub>S<sub>3</sub> hollow discoids with enhanced photoactivity. *Angew. Chem. Int. Ed.* **2014**, *126*, 6027–6031. [[CrossRef](#)]
62. Shi, L.; Wang, T.; Zhang, H.; Chang, K.; Meng, X.; Liu, H.; Ye, J. An amine-functionalized iron(III) metal-organic framework as efficient visible-light photocatalyst for Cr(VI) reduction. *Adv. Sci.* **2015**, *2*, 1500006. [[CrossRef](#)] [[PubMed](#)]
63. Yu, Y.; Yang, X.; Zhao, Y.; Zhang, X.; An, L.; Huang, M.; Chen, G.; Zhang, R. Engineering the band gap states of the rutile TiO<sub>2</sub>(110) surface by modulating the active heteroatom. *Angew. Chem. Int. Ed.* **2018**, *130*, 8686–8690. [[CrossRef](#)]
64. Zhang, Y.; Xu, M.; Li, H.; Ge, H.; Bian, Z. The enhanced photoreduction of Cr(VI) to Cr(III) using carbon dots coupled TiO<sub>2</sub> mesocrystals. *Appl. Catal. B Environ.* **2018**, *226*, 213–219. [[CrossRef](#)]
65. Deng, Y.; Tang, L.; Zeng, G.; Zhu, Z.; Yan, M.; Zhou, Y.; Wang, J.; Liu, Y.; Wang, J. Insight into highly efficient simultaneous photocatalytic removal of Cr(VI) and 2,4-dichlorophenol under visible light irradiation by phosphorus doped porous ultrathin g-C<sub>3</sub>N<sub>4</sub> nanosheets from aqueous media: Performance and reaction mechanism. *Appl. Catal. B Environ.* **2017**, *203*, 343–354. [[CrossRef](#)]
66. Butler, M.A. Photoelectrolysis and physical properties of the semiconducting electrode WO<sub>2</sub>. *J. Appl. Phys.* **1977**, *48*, 1914–1920. [[CrossRef](#)]

